Heterogeneous Catalysis Very Important Paper

International Edition: DOI: 10.1002/anie.201508571
German Edition: DOI: 10.1002/ange.201508571

Interface Engineering in Two-Dimensional Heterostructures: Towards an Advanced Catalyst for Ullmann Couplings

Xu Sun+, Haitao Deng+, Wenguang Zhu, Zhi Yu, Changzheng Wu, and Yi Xie*

Abstract: *The design of advanced catalysts for organic reactions is of profound significance. During such processes, electrophilicity and nucleophilicity play vital roles in the activation of chemical bonds and ultimately speed up organic reactions. Herein, we demonstrate a new way to regulate the electro- and nucleophilicity of catalysts for organic transformations. Interface engineering in two-dimensional heteronanostructures triggered electron transfer across the interface. The catalyst was thus rendered more electropositive, which led to superior performance in Ullmann reactions. In the presence of the engineered 2D Cu_2S/MoS_2 heteronanostructure, the coupling of iodobenzene and para-chlorophenol gave the desired product in 92 % yield under mild conditions (100 °C). Furthermore, the catalyst exhibited excellent stability as well as high recyclability with a yield of 89 % after five cycles. We propose that interface engineering could be widely employed for the development of new catalysts for organic reactions.*

The catalysis of organic reactions remains a vibrant field of scientific research and has attracted tremendous attention owing to its promising application in the synthesis of pharmaceuticals, agrochemicals, and organic electronic devices.[1–4] During most organic reactions, the electrophilic or nucleophilic surface of a catalyst activates chemical bonds and boosts the formation of intermediates, resulting in a decrease in activation energy of the reaction,[5–7] which accelerates the reaction. Various excellent and monodisperse catalysts for organic reactions, including enzymes, organocatalysts, and metal–organic frameworks (MOFs), have been intensively investigated; their electro/nucleophilicity is controlled either by induction or by conjugation effects.[8–13] In this regard, an ideal catalyst for organic reactions should display high stability, fine dispersity, and optimized electro/nucleophilicity.

Transition-metal chalcogenides (TMCs), with rich d electron configurations leading to controllable electronic structures, have experienced major development in the pursuit of novel catalyst designs.[14–20] Much effort has been devoted to engineering the surface and interface of TMC catalysts to enable diverse catalytic processes;[14,17,18–23] however, how to precisely manipulate their electro/nucleophilicity to be applicable for catalysis in organic reactions still remains a grand challenge. Interface engineering by forming 2D heteronanostructures of TMC catalysts with 2D nanomaterials[24,25] provides a new opportunity for optimizing the electro/nucleophilicity by interfacial effects.[26,27] Herein, we highlight a general route for the fabrication of 2D heteronanostructures, including Cu_2S/MoS_2, CdS/MoS_2, and FeS/MoS_2, by domain-matching epitaxial growth[28,29] of TMC materials on 2D MoS_2 nanosheets to form well-defined interfaces. We find that the 2D Cu_2S/MoS_2 heteronanostructure triggered a spontaneous electron transfer across the interface, which enhances the electron affinity of the catalytic surface and thus favors the attack of nucleophiles during the catalyzed reaction. As a proof of concept, the 2D heteronanostructure was tested in Ullmann couplings; the catalyst showed superior activity at low temperatures, excellent stability, durability, and high recyclability. Interface engineering in 2D heteronanostructures is thus a promising approach for optimizing the electro/nucleophilicity of the catalysts to improve their performance in organic reactions.

The general synthetic procedures for the 2D TMC/MoS_2 heteronanostructures are illustrated in Figure 1 a and b. After sonication in *N*,*N*-dimethylformamide (DMF), bulk MoS_2 was exfoliated into nanosheets with various sizes, among which the negatively charged large nanosheets provided the basic framework for the construction of the heteronanostructures. At first, the metal ions, M^{n+}, are attracted to the surface of the larger nanosheets owing to electrostatic interactions. Then, these M^{n+} ions will further react with S^{2-} to produce M_xS on the large MoS_2 nanosheets. It is understandable that these S^{2-} ions originate from the dissolution of the smaller MoS_2 nanosheets, which is assisted by the strong dipolar aprotic solvent DMF: the smaller nanosheets usually have a higher chemical potential and thus tend to dissolve; the dissolved ions will then diffuse and be transported to and grow on the surface of the larger nanosheets, which is similar to the Ostwald ripening process.[30] When the solution was heated with the magnetic stirrer set at 250 °C, M_xS was easily

---

[*] Dr. X. Sun,[+] H. T. Deng,[+] Z. Yu, Prof. C. Z. Wu, Prof. Y. Xie
Hefei National Laboratory for Physical Sciences at the Microscale
iChEM (Collaborative Innovation Center of Chemistry for Energy Materials), Hefei Science Center (CAS), and CAS Key Laboratory of Mechanical Behavior and Design of Materials
University of Science and Technology of China
Hefei, Anhui 230026 (P. R. China)
E-mail: czwu@ustc.edu.cn

Prof. W. G. Zhu
International Center for Quantum Design of Functional Materials (ICQD), Hefei National Laboratory for Physical Sciences at the Microscale (HFNL)
Synergetic Innovation Center of Quantum Information and Quantum Physics, University of Science and Technology of China
Hefei, Anhui 230026 (P. R. China)
and
Key Laboratory of Strongly-Coupled Quantum Matter Physics
Chinese Academy of Sciences, School of Physical Sciences
University of Science and Technology of China
Hefei, Anhui 230026 (P. R. China)

[+] These authors contributed equally to this work.

Supporting information for this article is available on the WWW under http://dx.doi.org/10.1002/anie.201508571.

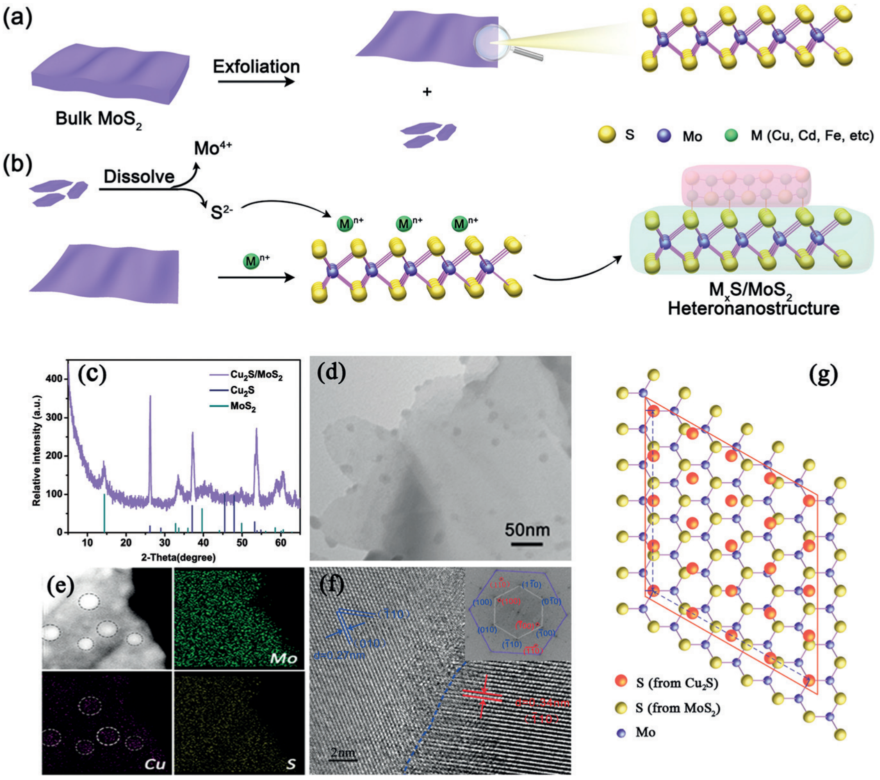

Figure 1. Synthesis and characterization of the 2D heteronanostructures. a, b) Synthetic route towards M$_x$S/MoS$_2$. c) XRD pattern of Cu$_2$S/MoS$_2$. d) TEM image, showing highly dispersed Cu$_2$S anchored onto MoS$_2$, resulting in the formation of the Cu$_2$S/MoS$_2$ 2D heteronanostructure. e) HAADF-STEM image and elemental mapping of Mo, Cu, and S for Cu$_2$S/MoS$_2$. f) HRTEM images of Cu$_2$S/MoS$_2$ and fast Fourier transform electron diffraction (FFT ED) patterns (inset). g) Domain-matching epitaxy of the as-formed Cu$_2$S/MoS$_2$ heteronanostructure.

anchored onto the larger MoS$_2$ nanosheets, forming 2D TMC/MoS$_2$ heteronanostructures with tunable electronic structures. In short, the epitaxial growth of TMC materials on 2D MoS$_2$ nanosheets constitutes a general route for the fabrication of 2D heteronanostructures, such as Cu$_2$S/MoS$_2$, CdS/MoS$_2$, and FeS/MoS$_2$, with well-defined interfaces.

Composition and morphology data of the as-synthesized Cu$_2$S/MoS$_2$ heteronanostructure are shown in Figure 1. The powder X-ray diffraction (XRD) patterns (Figure 1c) show two sets of diffraction peaks that could be readily indexed to MoS$_2$ (in turquoise, JCPDS No. 37-1492) and hexagonal Cu$_2$S (in blue, JCPDS No. 84-0206), which confirmed the successful growth of Cu$_2$S nanocrystals on the MoS$_2$ nanosheets. A transmission electron microscopy (TEM) image of Cu$_2$S/MoS$_2$ revealed that individual Cu$_2$S nanocrystals with a width of about 20 nm had been deposited on the MoS$_2$ nanosheets with no apparent aggregation (Figure 1d). Most of the nanocrystals were located at the edges of the MoS$_2$ nanosheets.[31,32] A HAADF-STEM image as well as the elemental mapping data confirmed the presence of elemental Cu and the uniform distribution of Cu$_2$S on the surface of the MoS$_2$ nanosheets, forming 2D Cu$_2$S/MoS$_2$ heteronanostructures (Figure 1e).

To obtain microstructural information on the heterostructure, high-resolution transmission electron microscopy (HRTEM) was carried out. A representative HRTEM image of the interface area of Cu$_2$S/MoS$_2$ shows two sets of lattice fringes, which correspond to MoS$_2$ and Cu$_2$S, respectively, further confirming that the two sides of the interface are composed of Cu$_2$S and MoS$_2$ (Figure 1f). The lattice distance of approximately 2.7 Å corresponds to the (100) and (010) lattice planes of hexagonal MoS$_2$. For the in situ formed Cu$_2$S nanocrystals, the measured lattice spacing was about 0.34 nm, which is in good agreement with the (100) planes of hexagonal Cu$_2$S, and sixfold symmetry similar to that of the MoS$_2$ substrate was observed. The fast Fourier transform pattern shows two sets of diffraction spots, which correspond to MoS$_2$ and Cu$_2$S (Figure 1f, inset). The first set of spots with well-defined hexagonal symmetry could be assigned to the (100) and (010) planes of MoS$_2$. The second set of spots with a lattice spacing of approximately 0.34 nm could be assigned to the (100) planes of Cu$_2$S, revealing the [001] orientation of the Cu$_2$S nanocrystals. The aforementioned analyses revealed that the ⟨100⟩ directions of Cu$_2$S are aligned with the ⟨100⟩ directions of MoS$_2$ while sharing a common [001] direction, which is due to the fact that the sulfur layers in these two samples hold the same hexagonal symmetry (see Figure 1g), favoring in-plane epitaxial growth.

The epitaxial relationship during the heterogeneous growth process can be explained in terms of domain matching.[28,29] For Cu$_2$S/MoS$_2$, the (100) spacing ratio between Cu$_2$S and MoS$_2$ was about 1.26, which is close to 5/4, implying that there are four Cu$_2$S unit cells per five MoS$_2$ unit cells. As a result, the mismatch[33] was as low as about 1.2%, thus enabling the in situ growth of Cu$_2$S nanocrystals on MoS$_2$ substrates by domain matching. Notably, the presence of 2D MoS$_2$ as a growth matrix also rendered hexagonal Cu$_2$S, which is usually observed at high temperatures, stable at room temperature. At room temperature, Cu$_2$S usually exists in the monoclinic phase known as chalcocite, and it would convert into hexagonal Cu$_2$S at temperatures above 105 °C. In Cu$_2$S/MoS$_2$, the stabilization of the high-temperature hexagonal Cu$_2$S phase is due to domain-matching epitaxial growth on the hexagonal MoS$_2$ lattice framework. Therefore, domain-matching epitaxy can stabilize hexagonal Cu$_2$S phases when immobilized on 2D nanosheets.

X-ray photoelectron spectroscopy (XPS) and Auger electron spectroscopy (AES) gave the valence states of the elements in the heteronanostructure. The XPS peaks corresponding to Mo 3d and S 2p are in accordance with previous reports,[34,35] demonstrating that no obvious changes in their valence states have occurred (Figure 2a, b). The high-reso-

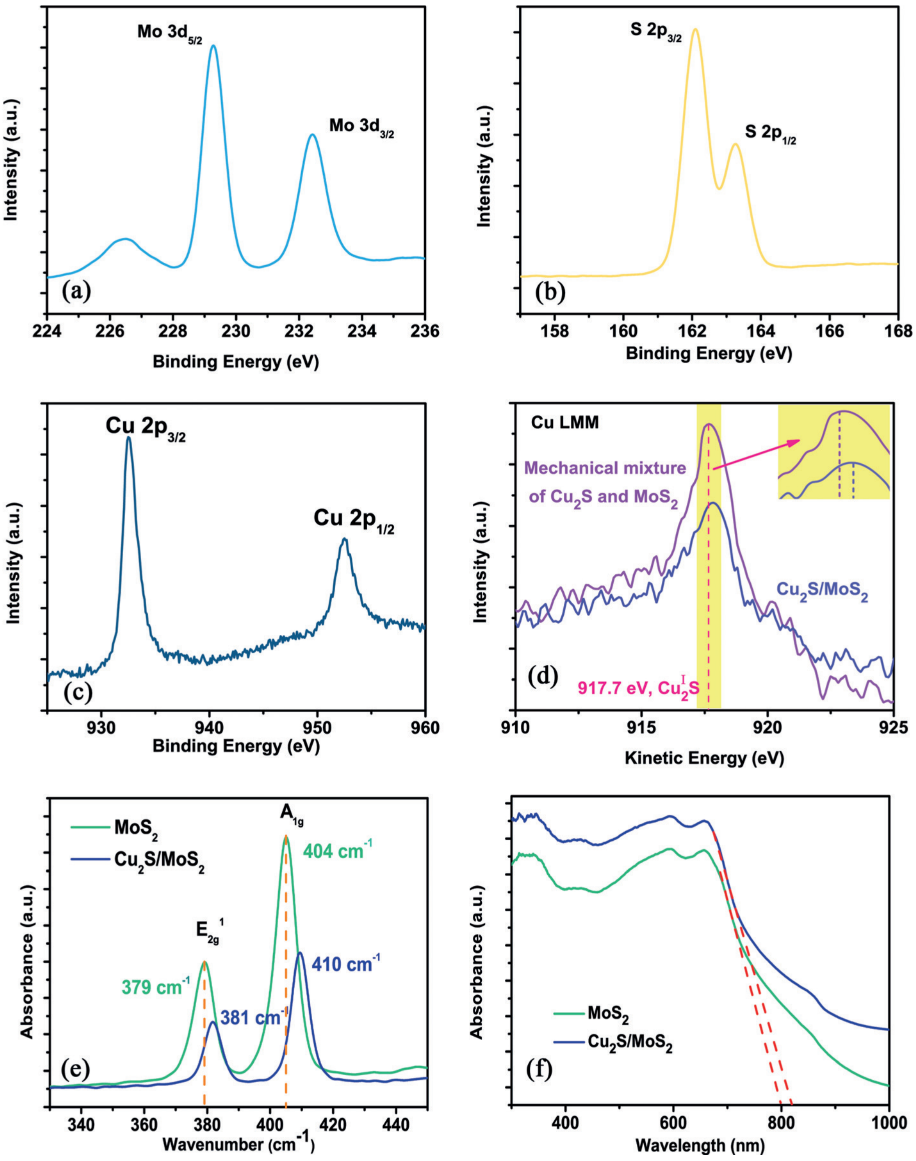

Figure 2. Spectroscopic characterization of the Cu$_2$S/MoS$_2$ heteronanostructure. a–c) XPS spectra for Mo, S, and Cu, respectively. d) LMM spectra of a mechanical mixture of Cu$_2$S and MoS$_2$ and the Cu$_2$S/MoS$_2$ heteronanostructure, revealing a slight positive deviation for the heteronanostructure (highlighted in yellow, magnified in the inset). e) Raman spectrum, showing blue shifts in the vibration modes. f) UV/Vis spectrum. A red shift of the absorption edge of Cu$_2$S/MoS$_2$ was observed, indicating substantial band-gap narrowing.

lution core spectrum of Cu 2p shows two obvious peaks with binding energies of approximately 932.4 eV and 952.6 eV, which could be assigned to Cu 2p$_{1/2}$ and Cu 2p$_{3/2}$, respectively (Figure 2c), excluding the possibility of Cu^{2+} formation because no satellite peaks were detected. However, as the Cu^{+} and Cu 2p peaks correspond to the same binding energy, the valence state of Cu could not be determined by the core 2p spectrum alone. The Auger electron spectrum (AES) in Figure 2d revealed the valence state to be +1, as the characteristic peak associated with LMM (Figure 2d, blue line) was close to that of Cu^{1+} according to a previous report.[35] This result confirmed the formation of a Cu$_2$S/MoS$_2$ heterostructure.

Furthermore, systematic characterization studies, for example, by Raman, UV/Vis, and AES spectroscopy, revealed the presence of interfacial effects in the 2D heteronanostructure. The Raman spectra revealed changes in the vibration modes for the 2D Cu$_2$S/MoS$_2$ heteronanostructure, confirming the above-mentioned hypothesis (Figure 2e). In detail, after immobilization of Cu$_2$S onto MoS$_2$, the in-plane vibration mode E$_{2g}{}^{1}$ and the out-of-plane vibration mode A$_{1g}$ had been blue-shifted compared to pristine MoS$_2$ (from 379 to 381 cm^{-1} for E$_{2g}{}^{1}$ and from 404 to 410 cm^{-1} for A$_{1g}$); the deviation in the A$_{1g}$ mode was larger. This could be attributed to the in situ growth of Cu$_2$S, which exploits the S layer of MoS$_2$ as an external S source, hence changing the primitive vibration mode of the Mo−S bonds, of which the out-of-plane vibration mode is altered more significantly. UV/Vis spectroscopy also provided evidence for electronic interactions (Figure 2 f), as the absorption edge of Cu$_2$S/MoS$_2$ showed band-gap narrowing in the combined system. The Cu LMM AES was much more intriguing (Figure 2d); the characteristic peak of Cu for Cu$_2$S/MoS$_2$ was found at 917.9 eV, whereas the peak for a mechanical mixture of Cu$_2$S and MoS$_2$ is located at approximately 917.6 eV. The slight positive deviation of 0.3 eV for the heteronanostructure compared to the mechanical mixture indicates a change in charge density on Cu^{I}, which could be related to interfacial effects. All of the spectra revealed the presence of strong interfacial effects in the Cu$_2$S/MoS$_2$ heterostructure.

To gain more comprehensive insight into the changes in the spectroscopic properties of the Cu$_2$S/MoS$_2$ heteronanostructure, we performed density functional theory (DFT) calculations to investigate the electronic structure upon interface formation. To model the Cu$_2$S/MoS$_2$ heterostructure, we constructed a supercell containing a 4 × 4 Cu$_2$S cell matching with a 5 × 5 MoS$_2$ cell, and a vacuum region of about 20 Å. The calculated density of states (Figure 3b) indicates that the Fermi level of the combined Cu$_2$S/MoS$_2$ system lies above the bottom of the conduction band of MoS$_2$, resulting in the injection of electrons from Cu$_2$S into MoS$_2$ upon contact. This is also consistent with the band diagram (Figure 3a) that was estimated by calculations on the isolated

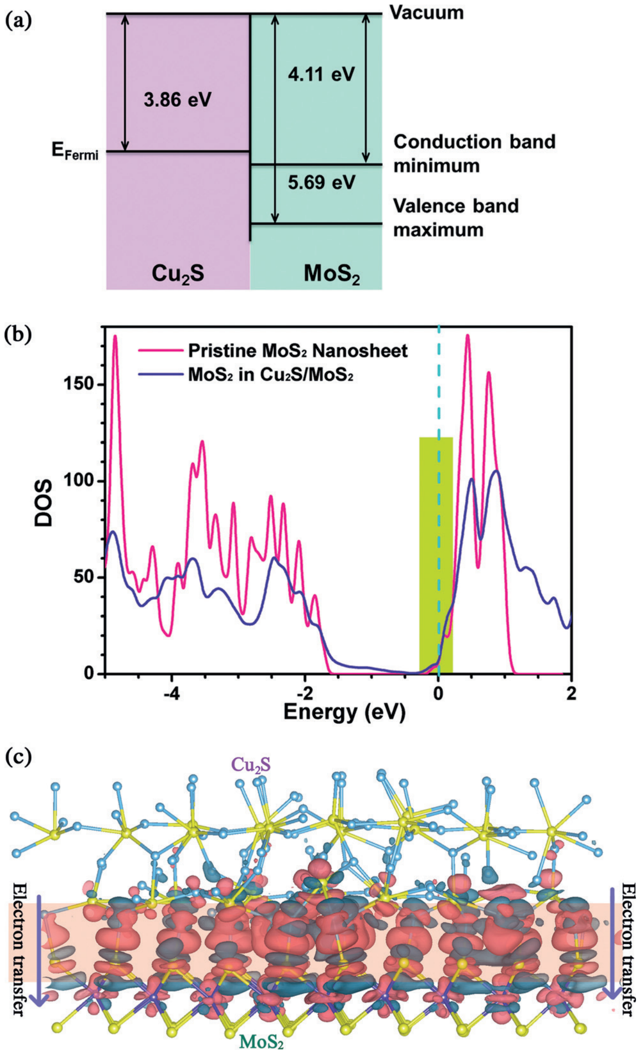

Figure 3. Calculated electronic structures of the Cu_2S/MoS_2 heteronanostructure. a) Band diagrams of MoS_2 and Cu_2S/MoS_2. b) The calculated total density of states of a pristine MoS_2 monolayer (pink) and the projected density of states for MoS_2 in the Cu_2S/MoS_2 heteronanostructure (blue). The Fermi level of the combined system is shifted to zero, as indicated by the dashed line, and the energy levels of the two systems are aligned with respect to the vacuum level. An increase in the density of states at the Fermi level is highlighted by the green region. c) The charge density difference in the 2D heteronanostructure of Cu_2S/MoS_2; dark red and dark blue represent regions of electron accumulation and depletion, respectively. The electron transfer from Cu_2S to MoS_2 is indicated by the blue arrow.

Cu_2S and MoS_2 systems. The projected density of states on MoS_2 from the heterostructure (Figure 3b, blue) shows substantial band-gap narrowing (in accordance with the UV/Vis spectroscopy results) and partial filling of the conduction band of MoS_2, in comparison with that of pristine MoS_2 nanosheets (pink). A more intuitive understanding can be obtained from the charge density difference image in Figure 3c. The accumulation and depletion of electrons mostly happen at the interface region, and the overall direction of such transfers is from Cu_2S to MoS_2 as indicated by the blue arrow. Such electron transfer ultimately leads to a reduced electron density in Cu_2S, which is revealed by the electron depletion around the Cu atoms, rendering the Cu^I atoms more electropositive.

As discussed above, electron transfer across the interface could render Cu^I more electropositive, resulting in enhanced eletrophilicity, which might facilitate the attack of nucleophiles during catalysis. For a proof-of-concept application, the Cu_2S/MoS_2 heteronanostructure was used as a catalyst in an organic reaction to understand how interfacial electron transfer influences the catalytic performance. The transition-metal ion Cu^+, with abundant 3d electrons, is a common catalyst for organic reactions.[36–40] The copper-catalyzed arylation of nucleophiles, the so-called Ullmann reaction, is a useful and practical method for the synthesis of various targets for the life sciences and polymer industries, and is pivotal in the formation of aryl carbon–carbon as well as aryl carbon–heteroatom bonds.[36,37] This process thus provides an opportunity to understand and manipulate the profound relationship between interfacial electron transfer and catalytic activity. In our case, the Cu_2S/MoS_2 heteronanostructure was found to benefit from interfacial electron transfer from Cu^I to Mo^{IV}, rendering Cu^I more electropositive, and thus holds great promise as a catalyst for Ullmann couplings (Figure 4a).

The catalytic performance of 5 wt% Cu_2S/MoS_2 in the coupling reaction of iodobenzene and *para*-chlorophenol was investigated in toluene solution in air at 100 °C (for results obtained under other conditions, see the Supporting Information, Table S1), and $CsCO_3$ was used as the base. After heating the reaction mixture to reflux at 100 °C for ten hours, the desired product had been formed in 92% yield (Table 1, entry 3), demonstrating that the Cu_2S/MoS_2 heterostructure is a good catalyst of this reaction and could even be a new type of ligand-free heterogeneous catalyst, which is significant for practical drug synthesis.[37] For comparison, the catalytic activities of a mechanical mixture of Cu_2S and MoS_2 and the individual components were tested as well, but they showed much lower or even no activity in this reaction (entries 1, 5, and 6). The catalytic efficiencies of 3 and 10 wt%

Table 1: Screening of various heterostructures as catalysts of the Ullmann reaction between iodobenzene and *para*-chlorophenol.

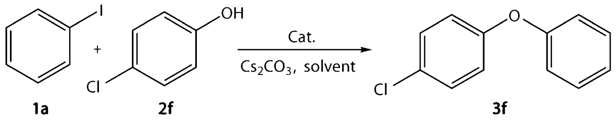

Entry	Catalyst	Yield [%]
1	Cu_2S+MoS_2	20
2	3 wt% Cu_2S/MoS_2	77
3	5 wt% Cu_2S/MoS_2	92
4	10 wt% Cu_2S/MoS_2	82
5	MoS_2	n.d.
6	Cu_2S	25
7	Cu	12
8	–	n.d.

Reaction conditions: **1a** (244 mg, 1.2 mmol, 1.2 equiv), **2f** (1 mmol, 1 equiv), toluene (2 mL), catalyst (10 mg), Cs_2CO_3 (388 mg, 1.2 mmol, 1.2 equiv), 100 °C, 10 h. Yields of isolated products were calculated based on the amount of **2f**. n.d. = not determined.

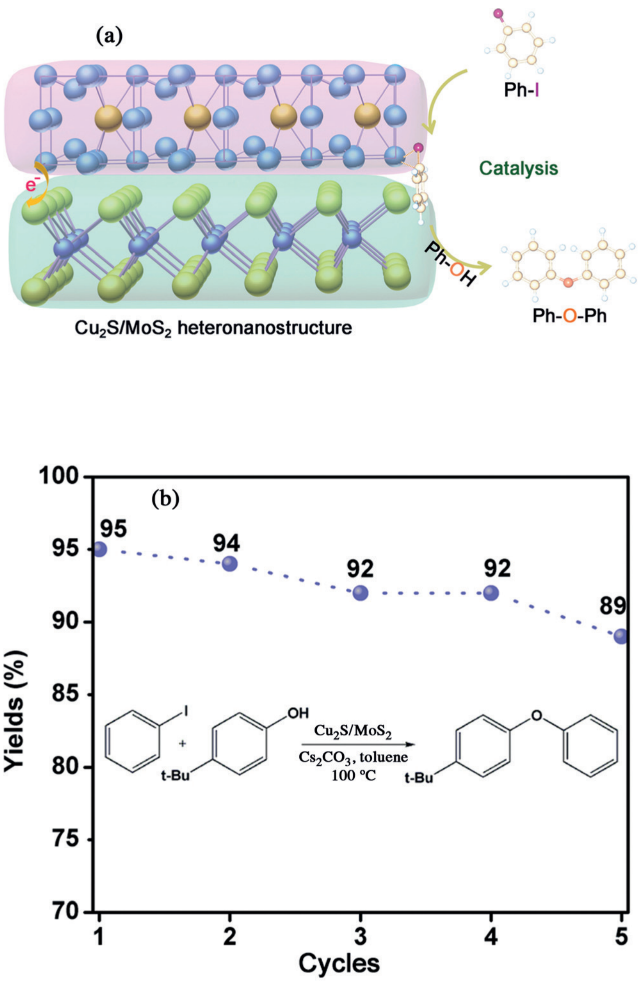

Figure 4. a) Cu_2S/MoS_2 as a catalyst of Ullman couplings. b) Yields obtained for different cycles and the Ullmann reaction that was carried out to test durability.

Cu_2S/MoS_2 were also determined under otherwise identical conditions (entries 2 and 4). Overall, 5 wt% Cu_2S/MoS_2 exhibited the best catalytic activity for the coupling of iodobenzene and *para*-chlorophenol. Therefore, all further reactions were conducted with this catalyst.

To explore the influence of different substituents on the coupling process, we analyzed the reactions of various phenol derivatives with iodobenzene. In all cases, the reactions proceeded with good efficiency, rendering the corresponding products in 70–95% yield (Scheme 1). The optimized electrophilicity, which is due to interfacial electron transfer, has greatly improved the catalytic activity of Cu_2S, leading to high reactivity at low temperatures.

The operational lifetime is also an important property of a catalyst. Compared to homogeneous catalysts, heterogeneous ones can be easily recycled, enabling sustainable industrial applications.[37] The durability of the Cu_2S/MoS_2 heteronanostructure was thus analyzed (Figure 4b). After recycling the catalyst five times, no apparent loss of activity was observed, with yields of around 90% in all five cycles. TEM images (Figure S5) of a catalyst sample that had been recycled five times (reactions at 100 °C) showed no obvious changes in morphology or aggregation of the Cu_2S nanoparticles, further confirming the high recyclability as well as dispersibility and substantiating the potential practical applications of this heteronanostructured catalyst. Compared with other catalysts,[36–40] apart from the high reactivity, which benefits from interfacial electron transfer, high recyclability was achieved owing to the use of 2D MoS_2 nanosheets as the catalyst support, which constitutes a more cost-effective approach for the design of catalysts of the Ullmann reaction and various other organic transformations.

In conclusion, engineering the interface of TMCs by forming 2D heteronanostructures has been shown to be a new route for controlling their electro/nucleophilicity. The heterostructure was shown to be an efficient catalyst for Ullmann couplings under mild conditions and displayed excellent stability and recyclability. The induced interfacial electron transfer in the 2D heteronanostructure increases the electron affinity of the catalytic surface, favoring the nucleophilic attack of the reactant during the catalytic process. We anticipate that interface engineering by the formation of heterostructures will be a powerful method for optimizing catalysts for various organic reactions and find various pharmaceutical and industrial applications.

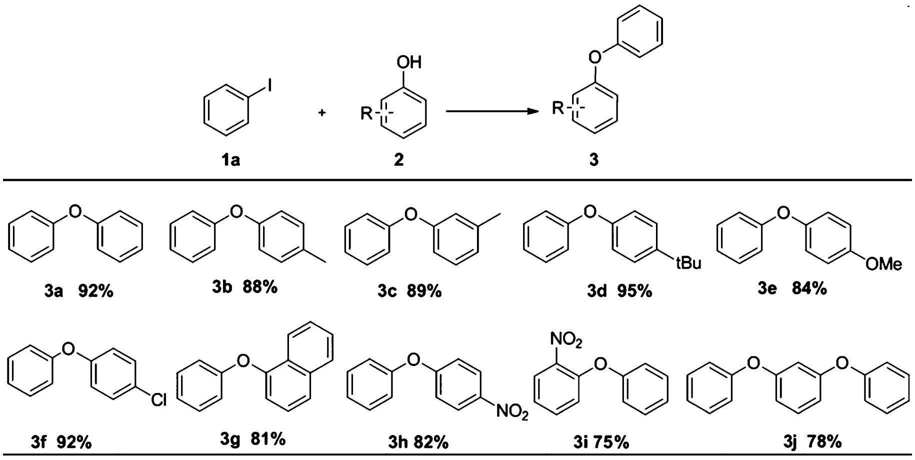

Scheme 1. Substrate scope of the Cu_2S/MoS_2 catalyzed Ullman coupling. Reaction conditions: **1a** (244 mg, 1.2 mmol, 1.2 equiv), **2** (1 mmol, 1 equiv), toluene (2 mL), 5 wt% Cu_2S/MoS_2 (10 mg, 0.1 equiv), Cs_2CO_3 (388 mg, 1.2 mmol, 1.2 equiv), 100 °C, 10 h. Yields of isolated products were calculated based on the amount of **2**.

Acknowledgements

This work was financially supported by the National Basic Research Program of China (2015CB932302), the National Natural Science Foundation of China

(21222101, U1432133, 11132009, 21331005, 11321503, J1030412, 11374273, and 11034006), the Chinese Academy of Science (XDB01020300), the Fok Ying-Tong Education Foundation, China (141042), and the Fundamental Research Funds for the Central Universities (WK2060190027, WK2090050027, and WK2340000063). Computational support was provided by the National Supercomputing Center in Tianjin.

Keywords: catalysis · electrophilicity · nucleophilicity · interface engineering · Ullmann reaction

How to cite: *Angew. Chem. Int. Ed.* **2016**, *55*, 1704–1709
Angew. Chem. **2016**, *128*, 1736–1741

[1] P. Laszlo, *Acc. Chem. Res.* **1986**, *19*, 121–127.
[2] A. S. K. Hashmi, *Chem. Rev.* **2007**, *107*, 3180–3211.
[3] J. S. Seo, D. Whang, H. Lee, S. Im Jun, J. Oh, Y. J. Jeon, K. Kim, *Nature* **2000**, *404*, 982–986.
[4] C. K. Prier, D. A. Rankic, D. W. MacMillan, *Chem. Rev.* **2013**, *113*, 5322–5363.
[5] M. L. Bender, *Chem. Rev.* **1960**, *60*, 53–113.
[6] D. Uraguchi, M. Terada, *J. Am. Chem. Soc.* **2004**, *126*, 5356–5357.
[7] T. Akiyama, K. Mori, *Chem. Rev.* **2015**, *115*, 9277.
[8] S. J. Benkovic, S. Hammes-Schiffer, *Science* **2003**, *301*, 1196–1202.
[9] R. Breslow, *Acc. Chem. Res.* **1995**, *28*, 146–153.
[10] T. W. Kelley, P. F. Baude, C. Gerlach, D. E. Ender, D. Muyres, M. A. Haase, D. E. Vogel, S. D. Theiss, *Chem. Mater.* **2004**, *16*, 4413–4422.
[11] H. Katz, A. Lovinger, J. Johnson, C. Kloc, T. Siegrist, W. Li, Y.-Y. Lin, A. Dodabalapur, *Nature* **2000**, *404*, 478–481.
[12] M. Yoon, R. Srirambalaji, K. Kim, *Chem. Rev.* **2011**, *111*, 1196–1231.
[13] B. S. Furniss, *Vogel's textbook of practical organic chemistry*, Pearson Education India, **1989**.
[14] J. Xie, J. Zhang, S. Li, F. Grote, X. Zhang, H. Zhang, R. Wang, Y. Lei, B. Pan, Y. Xie, *J. Am. Chem. Soc.* **2013**, *135*, 17881–17888.
[15] R. R. Chianelli, M. H. Siadati, M. P. De la Rosa, G. Berhault, J. P. Wilcoxon, R. Bearden, Jr., B. L. Abrams, *Catal. Rev.* **2006**, *48*, 1–41.
[16] J. Zhang, *PEM fuel cell electrocatalysts and catalyst layers: fundamentals and applications*, Springer Science & Business Media, Berlin, **2008**.
[17] S. Jeong, D. Yoo, J.-t. Jang, M. Kim, J. Cheon, *J. Am. Chem. Soc.* **2012**, *134*, 18233–18236.
[18] J. Chen, X. J. Wu, L. Yin, B. Li, X. Hong, Z. Fan, B. Chen, C. Xue, H. Zhang, *Angew. Chem. Int. Ed.* **2015**, *54*, 1210–1214; *Angew. Chem.* **2015**, *127*, 1226–1230.
[19] Z. Zeng, C. Tan, X. Huang, S. Bao, H. Zhang, *Energy Environ. Sci.* **2014**, *7*, 797–803.
[20] X. Huang, B. Zheng, Z. Liu, C. Tan, J. Liu, B. Chen, H. Li, J. Chen, X. Zhang, Z. Fan, *ACS Nano* **2014**, *8*, 8695–8701.
[21] C. Tan, H. Zhang, *Chem. Soc. Rev.* **2015**, *44*, 2713–2731.
[22] Z. Yin, B. Chen, M. Bosman, X. Cao, J. Chen, B. Zheng, H. Zhang, *Small* **2014**, *10*, 3537–3543.
[23] S. Harris, R. Chianelli, *J. Catal.* **1986**, *98*, 17–31.
[24] C. Tan, Z. Zeng, X. Huang, X. Rui, X. J. Wu, B. Li, Z. Luo, J. Chen, B. Chen, Q. Yan, *Angew. Chem. Int. Ed.* **2015**, *54*, 1841–1845; *Angew. Chem.* **2015**, *127*, 1861–1865.
[25] X. Huang, C. Tan, Z. Yin, H. Zhang, *Adv. Mater.* **2014**, *26*, 2185–2204.
[26] G. N. Vayssilov, Y. Lykhach, A. Migani, T. Staudt, G. P. Petrova, N. Tsud, T. Skála, A. Bruix, F. Illas, K. C. Prince, *Nat. Mater.* **2011**, *10*, 310–315.
[27] L. Li, X. Chen, Y. Wu, D. Wang, Q. Peng, G. Zhou, Y. Li, *Angew. Chem. Int. Ed.* **2013**, *52*, 11049–11053; *Angew. Chem.* **2013**, *125*, 11255–11259.
[28] X. Huang, Z. Zeng, S. Bao, M. Wang, X. Qi, Z. Fan, H. Zhang, *Nat. Commun.* **2013**, *4*, 1444.
[29] J. Narayan, P. Tiwari, X. Chen, J. Singh, R. Chowdhury, T. Zheleva, *Appl. Phys. Lett.* **1992**, *61*, 1290–1292.
[30] L. Ratke, P. W. Voorhees, *Growth and coarsening: Ostwald ripening in material processing*, Springer Science & Business Media, Berlin, **2013**.
[31] D. Voiry, A. Goswami, R. Kappera, C. de Carvalho Castro e Silva, D. Kaplan, T. Fujita, M. Chen, T. Asefa, M. Chhowalla, *Nat. Chem.* **2015**, *7*, 45–49.
[32] J. Kim, S. Byun, A. J. Smith, J. Yu, J. Huang, *J. Phys. Chem. Lett.* **2013**, *4*, 1227–1232.
[33] R. People, J. Bean, *Appl. Phys. Lett.* **1985**, *47*, 322–324.
[34] W. Zhou, Z. Yin, Y. Du, X. Huang, Z. Zeng, Z. Fan, H. Liu, J. Wang, H. Zhang, *Small* **2013**, *9*, 140–147.
[35] J. Zhang, J. Yu, Y. Zhang, Q. Li, J. R. Gong, *Nano Lett.* **2011**, *11*, 4774–4779.
[36] F. Monnier, M. Taillefer, *Angew. Chem. Int. Ed.* **2009**, *48*, 6954–6971; *Angew. Chem.* **2009**, *121*, 7088–7105.
[37] F. Monnier, M. Taillefer, *Angew. Chem. Int. Ed.* **2008**, *47*, 3096–3099; *Angew. Chem.* **2008**, *120*, 3140–3143.
[38] A. J. Paine, *J. Am. Chem. Soc.* **1987**, *109*, 1496–1502.
[39] J. E. Hein, V. V. Fokin, *Chem. Soc. Rev.* **2010**, *39*, 1302–1315.
[40] E. Corey, S. Knapp, *Tetrahedron Lett.* **1976**, *17*, 3667–3668.

Received: September 13, 2015